Nanoscale

PAPER

View Article Online
View Journal | View Issue

Cite this: *Nanoscale*, 2025, **17**, 25314

Heat-treatment-induced enhancement of activity and stability in Rh/Mo-doped PtNi octahedra for the oxygen reduction reaction

P. Paciok, *[a] S. Polani,[b] R. Amitrano,[b] T. Möller,[b] O. Prymak,[c] J. Kang,[b] M. Klingenhof,[b] K. MacArthur,[a,d] H. Matsumoto,[e] M. Heggen,[a] P. Strasser *[b] and R. E. Dunin-Borkowski [a]

Platinum-based bi- and trimetallic octahedral nanoparticles are among the most promising catalysts for the oxygen reduction reaction (ORR) at the cathode of proton exchange membrane fuel cells (PEMFCs). While these catalysts already exhibit excellent activity, their performance and durability can be significantly enhanced through reductive heat treatment and controlled doping. In this study, we investigate the structural and electrochemical evolution of Ni-rich PtNi and Mo/Rh-doped PtNi octahedra subjected to heat treatment in a hydrogen atmosphere. Rotating disk electrode (RDE) measurements reveal substantial improvements in both specific activity and long-term stability for the doped, heat-treated catalysts. Identical location scanning transmission electron microscopy (IL-STEM) confirms the exceptional morphological stability under accelerated aging conditions. *In situ* X-ray diffraction (XRD) and environmental STEM analyses attribute the enhanced performance to the formation of a thermodynamically stabilised Pt-rich skin. These findings highlight the dual role of dopants in preserving the active morphology and promoting beneficial surface segregation, offering valuable insights for the rational design of next-generation ORR catalysts for PEMFCs.

Received 13th May 2025,
Accepted 16th September 2025

DOI: 10.1039/d5nr01964h

rsc.li/nanoscale

Introduction

The planned transition away from fossil fuels in the areas of transportation, portable equipment, and stationary power generation to renewable and emission-free energy sources has led to an intensification of research in proton exchange membrane fuel cells (PEMFC).[1] Platinum-based materials are currently the benchmark catalysts for the sluggish oxygen reduction reaction (ORR) occurring at cathodes of industry-relevant PEMFCs.[2] In order to reduce the amount of expensive platinum and to increase the activity for the ORR, many design strategies have been investigated and published in the literature: one strategy is the incorporation of transition metals into the platinum lattice, which can lead to a reduction in material on the one hand and an increase in ORR activity by tuning the d-band centre on the other.[3] In addition to the composition and the resulting electronic effects, the morphology and surface of the catalysts also have a decisive influence on their activity.[4] Stamenkovic *et al.*'s pivotal work demonstrated the superior ORR activities of PtNi{111} single crystal surfaces, which subsequently drove significant research interest in faceted catalysts designed to maximise the percentage of {111} surfaces.[5] Pt_3Ni nanostructures with a Pt-skin have emerged as promising catalysts for ORR in fuel cells. The enhanced catalytic activity stems from a combination of strain and ligand effects. The compressive strain in the Pt-skin, induced by the lattice mismatch with the Ni-rich core, modifies the Pt d-band centre, optimising the oxygen adsorption energetics. Concurrently, the ligand effect, arising from subsurface Ni atoms, alters the electronic structure of surface Pt atoms, further tuning their catalytic properties. Based on this preliminary work, octahedral platinum–nickel catalysts with breakthrough activities were developed, whose performance could be further enhanced by adding another alloying element.[6–8]

Unfortunately, these promising catalysts have a fundamental flaw: in most published wet chemical syntheses of this class of catalysts, a platinum-rich seed forms first, followed by

[a]*Ernst Ruska-Centre for Microscopy and Spectroscopy with Electrons (ER-C), Forschungszentrum Jülich GmbH, Jülich 52425, Germany. E-mail: p.paciok@fz-juelich.de*
[b]*Electrochemical Energy, Catalysis and Material Science Laboratory, Department of Chemistry, Technical University Berlin, 10623 Berlin, Germany. E-mail: pstrasser@tu-berlin.de*
[c]*Inorganic Chemistry and Center for Nanointegration Duisburg-Essen (CENIDE), University of Duisburg-Essen, Universitaetsstr. 7, 45141 Essen, Germany*
[d]*Oxford Instruments Materials Analysis, High Wycombe, Buckinghamshire, UK*
[e]*Core Technology & Solutions Business Group, Hitachi High-Tech Corporation, 882 Ichige, Hitachinaka, Ibaraki 312-8504, Japan*

growth in all ⟨100⟩-directions, resulting in the formation of a hexapod.[9–11] Subsequently, the octahedral shape is established by filling in the {111}-facets with nickel. Since the nickel layer grows last and is not protected by a platinum shell, it is exposed to the acidic environment of the PEMFC and prone to dissolution, causing severe degradation during aging tests.[9,11] In addition to optimising the synthesis parameters to suppress or circumvent this segregation, the incorporation of additional alloying elements, and the application of heat treatments have shown promise to overcome the degradation effects.[12]

Recent studies confirm that doping Pt–Ni octahedra with select elements (such as Fe, Mo or Rh) can significantly improve both ORR activity and long-term stability. While the use of iron led to the retention of mass activity in accelerated aging tests, it simultaneously decreased the mass activity at the beginning of the lifetime by a factor of 8 compared to other PtNi catalysts.[13]

Huang *et al.* demonstrated a successful example of doping PtNi octahedra surfaces with Mo resulting in an increased activity and durability.[14] Beermann, Hornberger and Polani showed an increase in activity, stability and shape retention through alloying PtNi with Mo and Rh.[15–18]

To further increase long-term stability and minimise segregation, measures such as heat treatments were investigated. Heat treatments in vacuum or reductive atmospheres resulted in a decrease in the amount of nickel oxides on the particle surface and an accumulation of platinum on the {111} surfaces, which correlated with increased activity and stability.[19] Pan *et al.* applied heat treatments to Rh-doped PtNi octahedra and achieved an ORR mass activity of ~0.35 A mg_{Pt}^{-1} at 0.9 V and an exceptionally high power density of ~1.5 A cm^{-2} at 0.6 V in the membrane electrode assembly (MEA) test. The Rh doping proved effective in largely maintaining the octahedral particle shape even under load (improved morphological stability), while the increased Pt content resulted in a significantly higher current density.[20]

In this work, we present a novel approach to manipulate the surface structure and composition of octahedral PtNi nanoparticles by combining Rh and Mo doping and controlled heat treatment under a hydrogen atmosphere. Using *in situ* heating within a scanning transmission electron microscope (STEM) under gaseous environments, we reveal the remarkable surface transformation of the doped PtNi octahedra into a Pt-skin structure. This heat-induced process results in the formation of an ultrathin platinum shell encapsulating the octahedral particles. The synergistic effects of doping and the hydrogen atmosphere during heat treatment enable the creation of this distinct core–shell architecture, offering new possibilities for tailoring the catalytic properties of this system. Through real-time visualisation of these nanoscale structural transformations, our *in situ* heating experiments provide valuable insights into the complex interplay between composition, gaseous environments, and thermal dynamics in shaping nanoparticle architectures. These findings pave the way for rational design strategies to optimise the performance of PtNi nanoparticles in catalytic applications.

Results and discussion

Synthesis

Based on a synthesis route recently reported, different catalysts were prepared: a binary Ni-rich octahedral PtNi compound (denoted as PtNi-F, F: as prepared) and a Mo- and Rh doped PtNi octahedral catalyst (denoted as PtNiMoRh-F).[16] Details of synthesis and measurement protocols can be found in the SI. Elemental analysis *via* inductively coupled plasma optical emission spectroscopy (ICP-OES) showed a composition of 80% Ni and 20% Pt for the undoped PtNi-F. The use of dopants led to a lower Ni content of 65.6 at% in the PtNiMoRh catalyst particles. Hornberger *et al.* explained this observation with the presence of CO from the Mo precursor, which affects the growth and reduction kinetics of Pt and Ni. The presence of CO(g) inhibits the reduction kinetics of Pt(II) to Pt(0) and shifts the reaction equilibrium towards the precursor species. Consequently, this led to the formation of PtNiMoRh nanoparticles with increased dimensions relative to synthesis conditions without CO ligands.[16] Overall, the quaternary catalyst contained 0.4 at% Mo, 1.4 at% Rh, 32.6 at% Pt and 65.6 at% Ni as measured by ICP-OES. STEM analysis of the particles revealed average particle sizes of 6.97 nm ± 1.61 nm for the PtNi-F and 9.97 ± 2.27 nm for PtNiMoRh-F catalyst. In both samples, the {111} surfaces showed signs of concavity as reported by Gan and Polani (Fig. S2).[21,22] This may be due to the anisotropic octahedral growth, in which the deposition of the Ni-rich phase on the initially formed Pt-rich hexapods was not fully completed, leading to slightly concave Ni-rich {111} surfaces. In all samples, the number of octahedral particles was about 90%. Fig. 1 shows representative HR-STEM images and energy-dispersive X-ray spectroscopy (EDX) elemental maps of the octahedral particles. They all share a common feature, which can be interpreted as a hexapodal Pt-rich structure in the particle core.[10] Overview STEM images of the two samples at low magnification can be found in the Fig. S2 and S19.

EDX-maps also show the formation of an oxide layer on the particle surfaces. The thickness of the oxide layer corresponds to about 0.5 to 1 nm for the undoped catalyst. The oxide layer on the doped catalyst was considerably thinner and was in the range of 0.2 to 0.7 nm. The corresponding EDX-maps can be found in the SI (see Fig. S21–S24). X-ray photoelectron spectroscopy (XPS) analyses of the untreated catalysts also revealed a partial Ni oxidation (see Fig. S3). While 11.6 at% of the Ni in the sample PtNi-F was Ni(0), the amount in the sample PtNiMoRh-F dropped to 7.9 at%. Due to the segregation, the Ni, which was not covered by a protective Pt layer, was oxidised by ambient air after synthesis.[19] Fig. 1E and F show X-ray diffraction patterns of PtNi-F and its doped counterpart in their pristine state. According to the XRDs, the structures contain both Ni-rich and Pt-rich phases. For PtNi-F, 70 wt% of the active material has a composition of $Pt_{26}Ni_{74}$ with a lattice constant of 3.66 Å and 30 wt% of the material has a composition of $Pt_{57}Ni_{43}$ with a lattice constant of 3.80 Å. The average crystallite size for the Ni-rich phase is 3.2 nm and for the Pt-rich

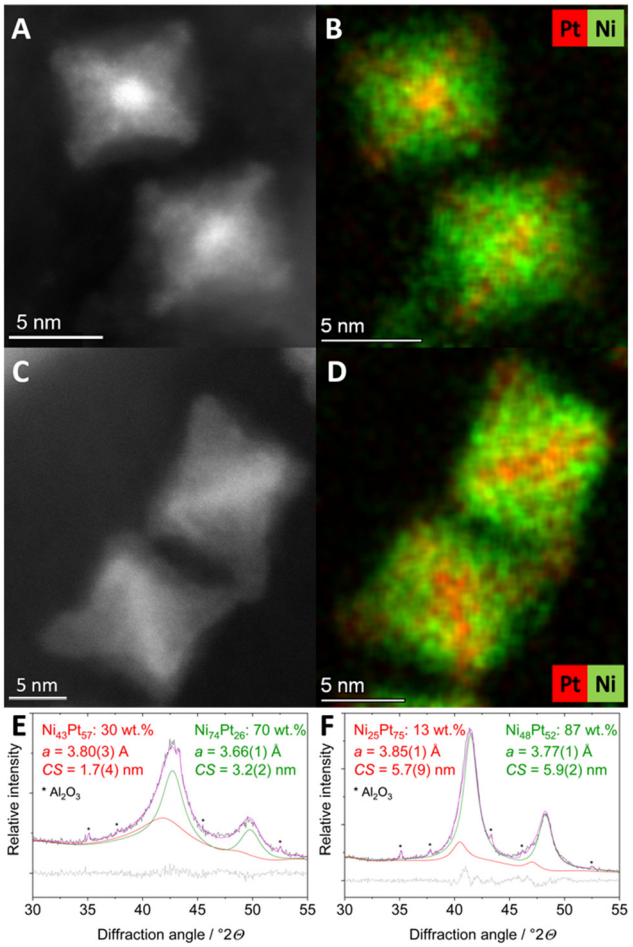

Fig. 1 Representative HAADF images of (A) undoped PtNi-F and (C) doped PtNiMoRh-F and their corresponding elemental maps (B and D) recorded at 80 kV. (E) XRD diffractogram of PtNi-F and (F) that of PtNiMoRh-F before heat treatment in a hydrogen atmosphere.

phase 1.7 nm. The proportion of Ni-rich species in PtNiMoRh-F is 87 wt% with an average crystallite size of 5.9 nm, with Pt-rich species proportion at 13 wt% and an average crystallite size of 5.7 nm. For the former phase the composition is $Pt_{48}Ni_{52}$ with a lattice constant of 3.77 Å and for the latter $Pt_{75}Ni_{25}$ with 3.85 Å. There are no reflections corresponding to a Ni oxide species, suggesting that the oxide layers are amorphous.

To shed light on the formation of the doped PtNi catalyst, a separate batch was prepared, heated and the reaction was stopped after 2 hours by quenching the reaction vessel. After 2 h reaction time, cuboctahedral Pt-rich particles with a diameter of 3.5 nm ± 0.7 nm and a composition of $Pt_{85}Ni_{15}$ have formed (see Fig. S4/S5). EDX measurements on various seed particles formed after this 2 h reaction time indicate the presence of rhodium in the formed seeds, but due to the high measurement error caused by the small amount of Rh used, only qualitative statements can be made (Fig. S5). Since the reduction potential of rhodium is more positive than that of Ni and is of the same order of magnitude as that of Pt, it seems plausible that rhodium is also deposited during the formation of the nuclei. Interestingly, both the PtNi seeds and the Pt-rich phase of the final synthesised doped PtNi octahedra display a similar composition.

Effects of reductive heat treatment on the physicochemical properties

The heat treatment had a significant impact on the physicochemical properties of the undoped PtNi catalyst. Overview images of both heat-treated catalysts can be found in the Fig. S6 and S19. For the heat-treated PtNi material (PtNi-H), the average particle size, which was determined by means of STEM HAADF images, increased from 6.97 nm ± 1.61 nm to 9.08 nm ± 4.34 nm. Moreover, the majority of the particles changed their morphology from octahedral to spherical. The heat-treated, Mo and Rh-doped PtNi material (denoted as PtNiMoRh-H) almost retained its average size distribution (8.92 ± 1.52 nm), the octahedral shape was mostly maintained and only the vertices showed a slight flattening or rounding. Also, to a small extent, particles in close contact began to show signs of agglomeration, but still retained their octahedral shape.

These observations indicated that the addition of molybdenum and rhodium led to an increase in stability against thermally induced diffusion processes that cause a loss of the octahedral shape.[23] The representative HAADF STEM images of the two heat-treated materials (Fig. 2) reveal the formation of a shell with higher HAADF image intensity towards the outside of the particles (denoted by X in the images). The HAADF image intensity varies proportionally with the atomic number Z.[24] Platinum (Z = 78) and nickel (Z = 28) are sufficiently different in atomic number that the heavier Pt-rich regions will appear brighter in the image than Ni-rich regions. This observation indicates a formation of a Pt-rich shell during the heat treatment in a hydrogen rich atmosphere. The EDX maps of the heat-treated PtNi material show a random or almost disordered localisation of the Pt within the particle structure indicating a loss of the inner hexapod structure. In contrast, this structure can still be found in the doped heat-treated PtNiMoRh-H material. The EDX elemental maps also indicate the formation of a Pt shell for both heat-treated materials. Regardless of the initial particle composition, the heat-treatment induced a Pt-rich shell with a diameter of 0.4 to 0.9 nm for the PtNi-H material and 0.1 nm to 0.4 nm for the doped material. Interestingly, the PtNi-H as well as some PtNiMoRh-H particles exhibit signs of a Ni oxide layer after heat treatment following exposure to the ambient atmosphere. Contact with oxygen triggers Ni segregation. As this effect is more pronounced with PtNi-H, it appears that either the Pt layer formed is unable to prevent Ni segregation, the Pt layer was not uniformly formed and exhibits pinholes, or the combination of a Pt layer and doping with Mo/Rh also prevents oxygen-induced Ni segregation.

The effect of heat treatment on the crystal structure and phase composition was further elucidated using XRD (Fig. 2). After heat treatment, the Pt-rich phase disappeared and the

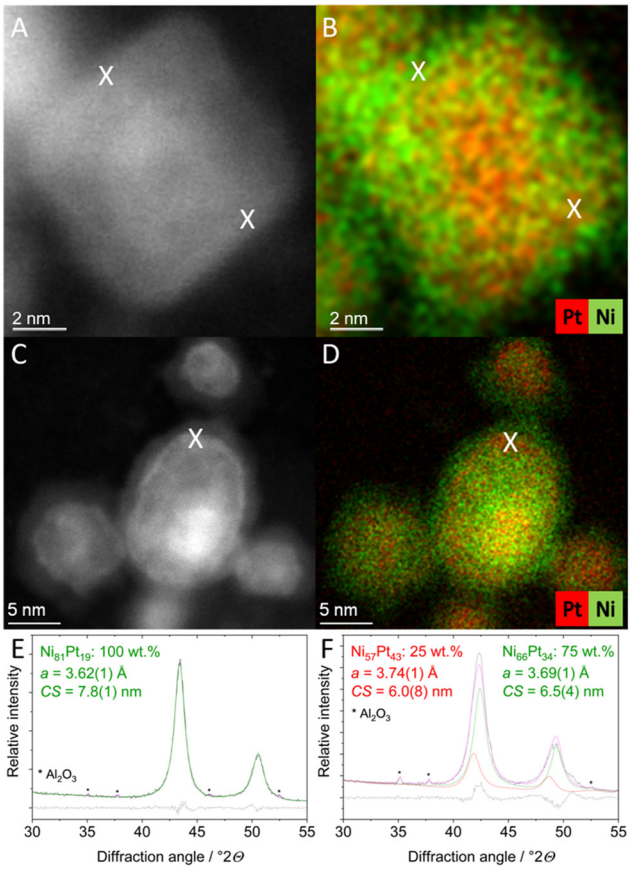

Fig. 2 Representative HAADF images of (A) doped PtNiMoRh-H and (C) undoped PtNi-H and their corresponding elemental maps (B and D) recorded at 80 kV. (E) Shows the XRD diffractogram of PtNi-H and (F) that of PtNiMoRh-H after heat treatment in a hydrogen atmosphere. (X) Marks the formation of a platinum layer.

PtNi-H material consisted of only one phase, $Pt_{19}Ni_{81}$, with a crystallite size of 7.8 nm and a lattice constant of 3.62 Å. This reflects the results of the STEM/EDX study, as the Pt-rich hexapod structure disappeared due to the formation of a single PtNi phase. In contrast, after heat treatment, the doped material still had two phases: a Ni-rich phase with a composition of $Pt_{34}Ni_{66}$, a lattice constant of 3.69 Å and a crystallite size of 6.5 nm and a Pt-rich phase with a composition of $Pt_{43}Ni_{57}$, a lattice constant of 3.74 Å and a crystallite size of 6 nm. A reduction in the lattice constant is observed in both heat-treated materials, which is explained by an increase in the Ni content. During the characterisation of the two untreated materials PtNi-F and PtNiMoRh-F using STEM/EDX, an amorphous Ni oxide layer could be seen on the surface of the particles. Due to the heat treatment, the Ni oxide was reduced and integrated into the other phases after diffusion.

XPS analysis of both heat-treated materials revealed a twofold increase in Ni(0) after the treatment, which aligned well with observations from other heat-treated PtNi-based materials.[19]

Taken together, these results indicate that the core of the PtNiMoRh nanoparticles is best described as a Pt–Rh-rich hexapod framework rather than a fully intermetallic phase. The annealing at 350 °C in H_2/Ar preserves this Pt–Rh hexapod in the doped system, whereas the undoped PtNi octahedra lose it due to interdiffusion. Thus, Rh and Mo act synergistically to stabilise the inner Pt–Rh skeleton and prevent full intermetallic ordering or collapse.

Electrochemistry

The activity and stability of the as-synthesised and heat-treated materials are summarised in Fig. 3. The electrochemical surface area (ECSA) assessment was carried out using H_{upd} and CO adsorption, but in the following only the values based on CO adsorption are utilised, as H_{upd}-based values underestimate the ECSA and thus lead to errors in the specific activity (SA) determination. An ECSA of 66 $m^2\ g^{-1}$ was determined for PtNi-F and an ECSA of 56 ± 6.7 $m^2\ g^{-1}$ for PtNiMoRh-F, which agrees well with ECSAs of similar particles.[14,16] The heat treatment of PtNi-F led to a 43% reduction in its ECSA, which is explained by a morphological change and agglomeration of the octahedra, an increase in the particle size distribution and the resulting poorer surface-to-volume ratio. Heating the doped PtNi material on the other hand increased the ECSA by almost 30%. This enormous gain in ECSA can be explained on the one hand with the removal of Ni oxide species on the surface, on the other hand, due to the formation of a Pt shell, the amount of active Pt on the surface was increased.[25,26] The change of the ECSA taking place during accelerated stress test (AST) is an excellent indicator for the assessment of the catalyst stability. To probe the stability of the materials, ASTs were carried out in the potential range from 0.6 to 0.95 V_{RHE} with 10 800 cycles. While the cycling of the pristine PtNi material led to a 17% reduction in ECSA, the effect of AST on the ECSA of the other materials was negligible, indicating the improved stability of the doped PtNi material and the positive effect of Pt shell formation on particle stability. CO stripping measurements provided further insight into the surface structure of the catalysts. PtNi-F and PtNi-H exhibited a single CO oxidation peak centred at 0.71 V_{RHE}, whereas PtNiMoRh-F and PtNiMoRh-H displayed an additional pre-peak at around 0.51 V followed by the main oxidation peak at 0.71 V. The appearance of such low-potential features is commonly attributed to heterogeneous surface sites or residual subsurface Ni, which supply OH species at lower potentials and facilitate CO oxidation. The main peak at 0.71 V is negatively shifted compared to commercial Pt/C (~0.78–0.80 V), which is in agreement with a compressively strained Pt-skin.[27]

A comparison of the ECSA derived from H_{upd} and CO stripping further supports this interpretation. For PtNiMoRh-H, the $ECSA_{CO}$ exceeded the $ECSA_{Hupd}$ by nearly a factor of 1.5, which is consistent with previous reports on Pt-skin structures where H adsorption is weakened due to compressive strain.[28] The undoped PtNi-H showed nearly identical H_{upd}- and CO-based ECSA values, suggesting the absence of a well-defined Pt-skin. Moreover, STEM analysis revealed that the Pt shell in PtNi-H is considerably thicker (0.4 to 0.9 nm) compared to the doped material (0.1 to 0.4 nm). Considering that one atomic layer of

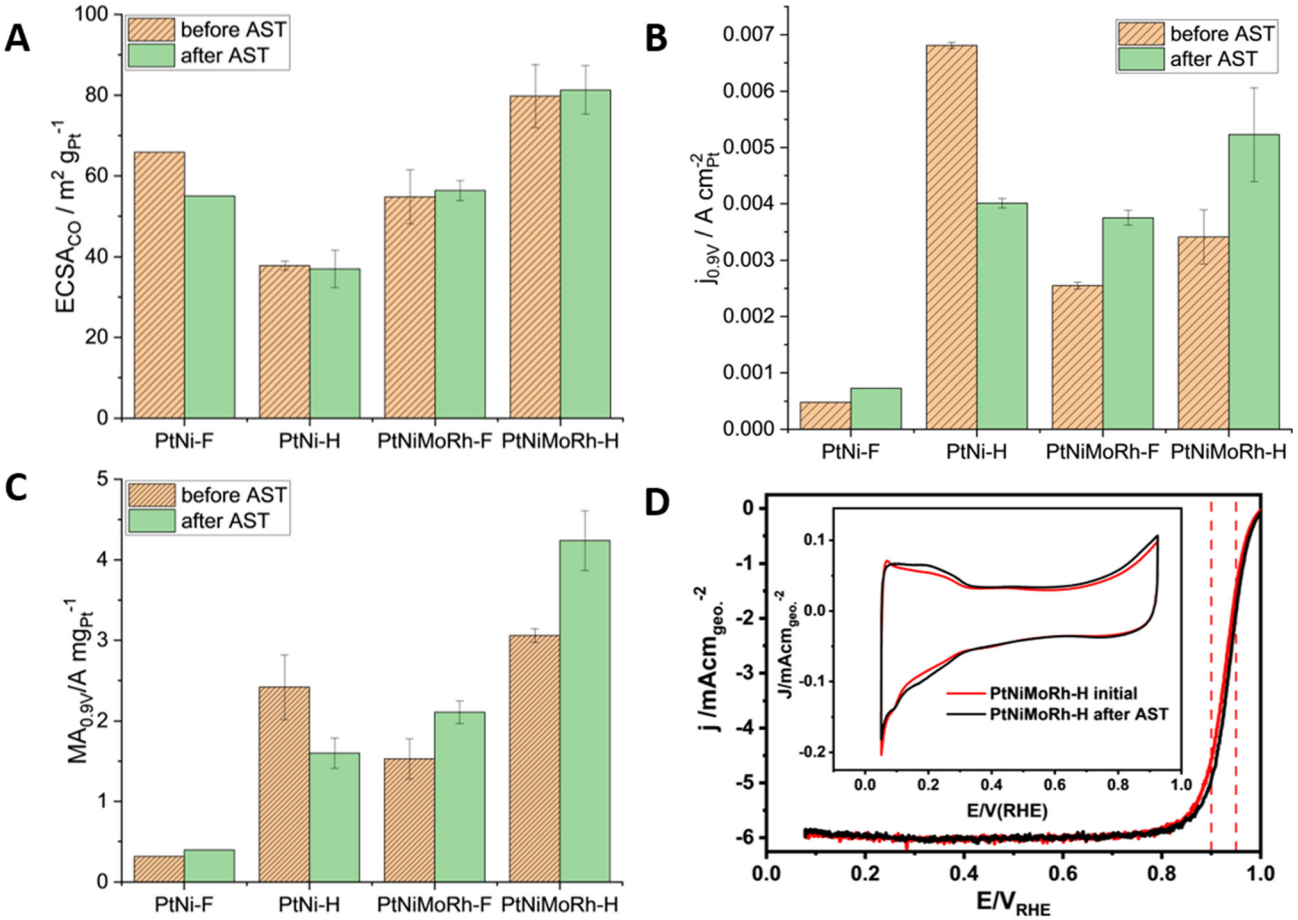

Fig. 3 Summary of the electrochemical evaluation: (A) $ECSA_{CO}$, (B) specific activity (based on $ECSA_{CO}$) and (C) mass activity evaluated at 0.9 V_{RHE} before and after the AST. (D) Linear sweep voltammetry curves (rpm 1600, scan rate 20 mV s^{-1}) before and after the AST (10 800 cycles between 0.6 and 0.95 V_{RHE} at a scan rate 1 V s^{-1}) in 0.1 M $HClO_4$ at RT. Inset shows the cyclic voltammetry profile before and after the AST. The other corresponding linear sweep voltammograms and cyclic voltammograms, as well as the respective values, are summarised in tabular form in the Fig. S17, S18 and Tables S1, S2.

Pt(111) corresponds to around 0.23 nm, this means that the undoped material is covered by around 2–4 atomic layers of Pt, while the doped catalyst is limited to around 1–2 layers. Such thicker shells are known to gradually lose the beneficial strain and ligand effects from the Ni-rich core, and therefore behave electrochemically more similar to pure Pt. This explains the lower specific activity of PtNi-H despite the apparent formation of a Pt-rich overlayer.[29]

For the activity determination, the SA and MA were assessed. In the case of the PtNi material, there was a sharp increase in SA and MA after the heat-treatment due to a restructuring of the surface forming a Pt-skin, and an increase in particle size due to a change of the crystallite phase.

For the doped material, an increase in SA and MA was also observed, but to a lesser extent. While applying AST to the heat-treated undoped PtNi-H material caused a sharp decline in the SA and MA, cycling of the pristine (PtNiMoRh-F) and heat-treated doped material (PtNiMoRh-H) led to an increase in activity. Since the ECSA of PtNi-H, PtNiMoRh-F and PtNiMoRh-H showed negligible changes after AST, the decrease in SA can likely be attributed to changes in the catalyst surface composition.

To further probe the ORR mechanism, we derived Tafel plots from the ORR polarization curves at 1600 rpm (see Fig. S29). The resulting slopes are in the range of 50–53 mV dec^{-1}, consistent with typical values for Pt-based alloys in acidic electrolyte.[30,31] Within the uncertainty of the fits, no statistically significant differences between the catalysts could be resolved. Together with the diffusion-limited currents and onset potentials, these results support that all investigated catalysts follow the expected $4e^-$ ORR pathway. The contrasting trends between ECSA and SA/MA can be rationalized by the structural changes upon annealing: while undoped PtNi octahedra lose their {111} facets and activity, Rh/Mo-doping stabilizes the octahedral shape, thereby preserving a higher intrinsic activity.

Degradation assessment *via* identical location STEM

The effect of the AST on the four different catalyst systems was analysed *via* Identical Location Scanning Transmission

Electron Microscopy (IL-STEM)/EDX. The IL-STEM technique is a powerful tool for investigating the structural and morphological evolution of electrocatalysts under accelerated aging tests, particularly in the context of the oxygen reduction reaction (ORR). By enabling high-resolution imaging of the same nanoscale region before and after electrochemical cycling, IL-STEM provides critical insights into degradation mechanisms such as particle dissolution, coalescence, and support corrosion. This approach minimises sample variability and allows for a direct correlation between catalyst performance loss and structural changes, making it indispensable for the development of durable ORR catalysts.[32] The AST was conducted in Ar-saturated 0.1 M $HClO_4$ with 10 800 cycles between 0.6 and 0.95 V_{RHE} at a scan rate of 1 V s^{-1}. Fig. 4 shows the comparison of the initial and aged state of the PtNiMoRh-H catalyst after cycling in Ar-saturated 0.1 M $HClO_4$. Comparative images of the other catalysts before and after the AST at identical locations can be found in the Fig. S8, S10, S12 for HAADF images/EDX maps; Fig. S9, S11, S13 and S20. In the untreated PtNi-F catalyst, cycling resulted in dissolution of the Ni-rich facets and formation of a Pt-rich skeleton causing a loss of the octahedral shape. The average relative Ni loss was measured using EDX and amounted to 32.4% ± 4.3%. Cycling of the heat-treated PtNi catalyst resulted in relative Ni loss of 6.1% ± 3.4%, but the particles retained their spherical shape and the Pt shell remained intact.

In general, the removal of Ni from the surface layers results in a reduction in the geometric and electronic effects of Ni on Pt, which, with an ideally adjusted Pt–Ni ratio, contribute to an improved adsorption behaviour of oxygen on Pt and thus to an increase in activity. Since this is no longer the case for the cycled PtNi-F due to the diminishment of Pt in the outermost layers, the activity converges to that of pure Pt. Although Ni is still present in deeper layers, it can no longer exert any effect on the outermost Pt layer above a certain thickness.[33] After applying ASTs to the untreated PtNiMoRh-F, the general morphology of the octahedral form remained mostly unchanged. The elemental distribution of Pt in the Pt-rich hexapod shape was preserved and Ni on the facets was leached to a small extent, resulting in the concavity of the octahedral particles becoming more pronounced. Due to the low concentration of Mo and Rh dopants, their distinct localisation and local concentration could not be determined either before or after the ASTs, while Ni exhibited a relative loss of about 8% ± 8%. IL-STEM analysis of the heat-treated PtNiMoRh catalyst showed no morphological or structural change in the octahedra. Only the mean EDX-measured Ni content decreased to a minor extent. Notably, in all four samples analysed by IL-STEM no movement of the particles was observed during cycling. All particles remained localised in the same places and no particle detachment could be detected. This is in contrast to other IL-(S)TEM studies carried out on "standard" Pt/C. Overall, the heat-treated PtNiMoRh-H particles show exceptional morphological stability after the AST.

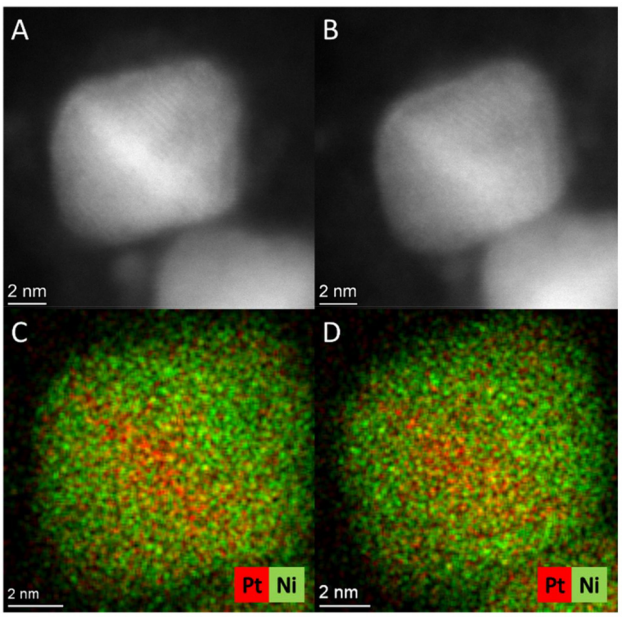

Fig. 4 Representative HAADF-STEM images and their corresponding EDX elemental maps of PtNiMoRh-H octahedra before (A) and after (B) 10 800 AST cycles (06–0.95 V_{RHE}) at the identical location and their corresponding EDX elemental maps (C and D).

In situ STEM evaluation of the Pt skin formation

To gain a deeper understanding of the process occurring during the heat-treatment of the PtNi-based octahedra in a hydrogen atmosphere, *in situ* heating experiments in an environmental STEM (Hitachi HF5000) were performed. Prior to the actual heating experiments, the samples were heated inside the microscope at 200 °C for 30 min to remove possible organic contaminants. A temperature of 300 °C was selected for the *in situ* experiments, as a significant reduction of Ni and diffusion of Pt was expected only above this temperature.[19] Subsequently, several sample sites were pre-characterised, hydrogen was admitted into the microscope column, and the temperature was increased to 300 °C with a ramp of 3 °C s^{-1}. To minimise the interaction of the electron beam with the sample, images were recorded every 5 min. Fig. 5 shows a representative PtNiMoRh-H particle during *in situ* heating at four different stages. A more extensive series of images can be found in the SI. In the initial state (t = 0 min), Fig. 5A shows a particle lying in the {110} zone-axis, the internal hexapod structure is clearly visible, as well as spherical Pt-rich deposits at the vertices. After 5 minutes, the accumulations at the vertices taper off and the excess material migrates to the {111} surfaces (Fig. 5B). After further 5 minutes, a flattening of the edges, a change in the outermost atomic layers and a refilling of the {111} facets was observed (Fig. 5C). Over the course of a few minutes, the contrast of the surface atomic layers increased sharply compared to the rest of the inner material, which is a strong indication of Pt enrichment. At the same time, the contrast of the next two atomic layers below decreased sharply compared to the underlying material, which indicates a depletion of Pt or an enrichment of Ni (Fig. 5D). *Ex*

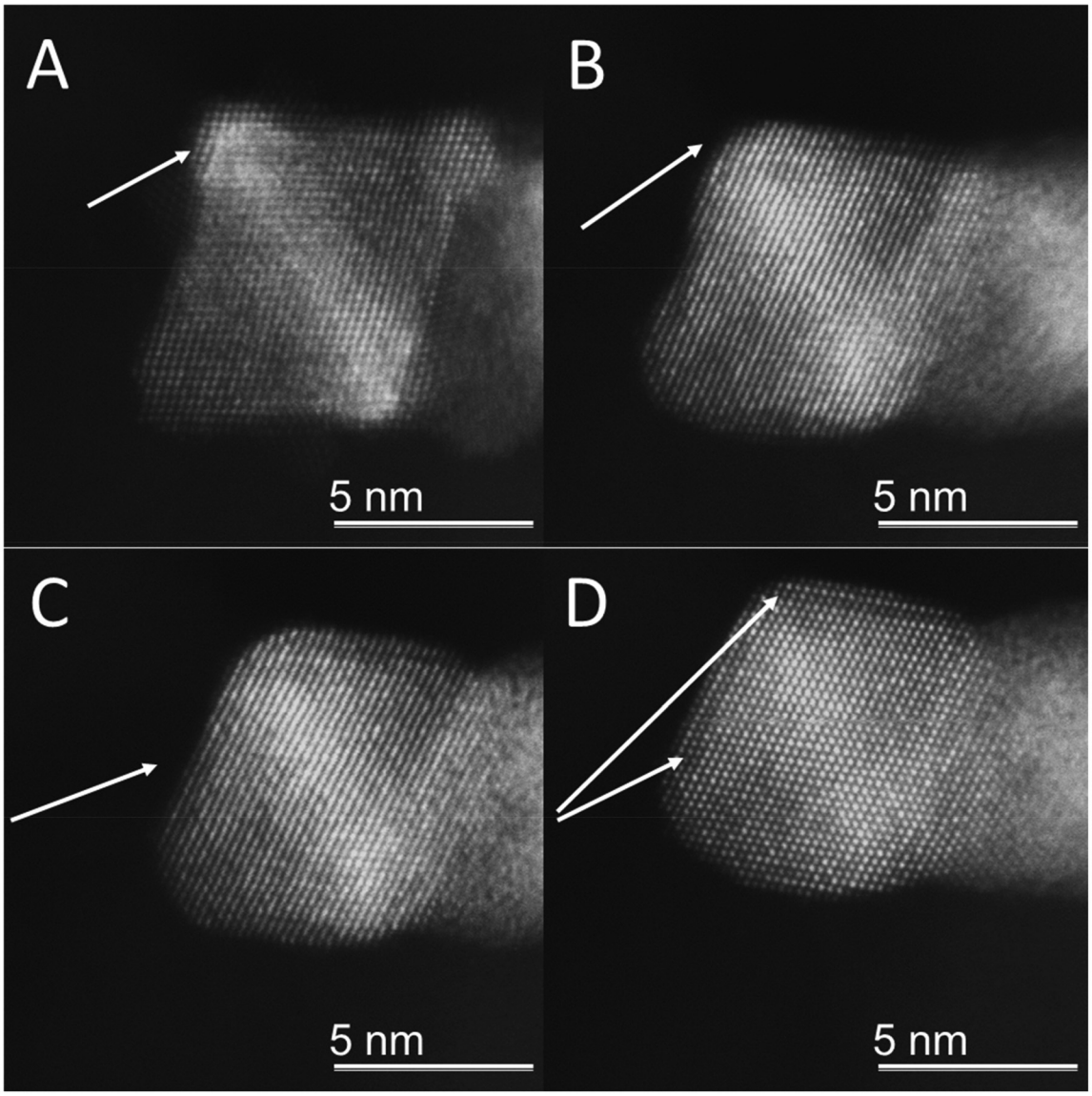

Fig. 5 *In situ* snapshots of the structural evolution of doped PtNiMoRh octahedra during heat treatment in a hydrogen atmosphere. The images were taken in an environmental STEM at a temperature of 300 °C and a hydrogen pressure of approx. 5 Pa. To minimise the influence of the beam, the images were recorded every 5 minutes. (A) Shows the initial state, (B) after 5 min, (C) after 30 min and (D) after 60 min. A more extensive series of images can be found in the SI (see Fig. S14).

situ EDX measurements of comparable particles also showed that Pt was enriched in the outer atomic layers of the octahedron and Ni in the layers below. With further heating, the vertices became rounder and less pronounced. After increasing the temperature to 350 °C, the curvature of the corners became more pronounced, but the thickness of the Pt-enriched layer remained unchanged. In the case of undoped octahedra (Fig. S16), material from the corners migrated to the edges while the intensity of the hexapod structure in the particle interior declined and a rounding towards spherical particles was observed. The loss of the hexapod structure was a clear indication of Pt and Ni mixing accompanied by the formation of a new PtNi phase, which agrees well with the XRD results. Similar to the doped octahedra, the pure PtNi material also formed a Pt-rich layer. Due to the breakdown of the octahedral particle structure and the formation of a new PtNi phase, more Pt was present, which could diffuse outwards due to the effects of temperature and hydrogen, where it contributed to the formation of a thicker Pt shell compared to the doped PtNiMoRh-H. In the case of PtNiMoRh-H, the stable Pt-rich hexapod resulted in less Pt being able to diffuse outwards, leading to a thinner Pt shell. Another important observation that underlines the structure-stabilising properties of rhodium on Pt is the formation of agglomerates of closely spaced PtNi octahedra. While the particle structure was largely preserved in the agglomeration of doped PtNi octahedra and only a

merging of the adjacent edges was detected, a loss of the octahedral structure was observed in undoped PtNi particles with immense particle diameter growth. Upon comparing the HAADF images of the two *ex situ* treated samples with the *in situ* electron microscopy data, we observed minimal to negligible differences. Consequently, we conclude that the alterations in catalyst materials observed *in situ* can be attributed solely to heat treatment in a hydrogen atmosphere, with electron beam effects playing no significant role.

Formation of a Pt skin

As demonstrated by high-resolution *ex-* and *in situ* STEM images, heating PtNi and Mo/Rh-doped PtNi in a hydrogen atmosphere causes the formation of a Pt-rich skin on the particle surfaces, regardless of the presence of Rh or Mo. The formation of the Pt-rich skin can be attributed to different processes: reduction of surface Ni oxides, followed by a temperature and hydrogen induced surface segregation. Due to the Ni-rich nature of the octahedra and the Pt/Ni segregation present after the synthesis, the surface Ni is oxidised by ambient air as evident from the STEM/EDX images in Fig. S14 and was also observed by other authors.[12,34,35] A further enrichment of the surface with Ni is also driven by oxygen adsorption. The driving force for the oxygen induced Ni segregation is, on the one hand, the reduction in strain caused by a lattice mismatch of Pt and Ni and, on the other hand, the lower surface energy of NiO compared to Pt and the strong interaction between NiO and Pt.[36]

Based on the STEM images in Fig. 5A, Ni oxide reduction proceeds quite rapidly, which was also observed in *in situ* TEM/EELS and *in situ* XRD studies by other authors.[37,38]

Furthermore, Wang *et al.* analysed the reduction behaviour by DFT methods and showed that by reducing the surface Ni oxide species to Ni(0), removing adsorbed oxygen, and by adsorption of hydrogen, the Pt–Pt and Pt–Ni bonds are weakened, thus promoting Pt segregation to the surface.[39]

Thermal treatment under hydrogen atmosphere at 350 °C results in the reduction of surface Ni oxide to metallic Ni and simultaneously induces the diffusion of a small fraction of surface Ni atoms into subsurface layers. Due to the lower surface energy of Pt (1.49 J m^{-2}) compared to Ni (1.92 J m^{-2}), Ni surface atoms exhibit a tendency to diffuse into the subsurface, while Pt atoms segregate to the topmost atomic layers during annealing processes in vacuum or under reducing conditions.[36,40–42] In addition to this, Pt located at the vertices migrates to the {111} facets also taking part in the formation of a Pt skin. This is rationalised by the undercoordinated nature of the vertices' Pt atoms.[43] Due to hydrogen adsorption and the following weakening of the Pt–Pt and Pt–Ni bonds a migration of Pt to more stable sites occurs.[44]

Rhodium and molybdenum induced shape stability

The STEM and XRD *in situ* data reveal that not only the particle shape of the PtNi octahedra is preserved by the addition of Mo and Rh, but also the Pt-rich hexapod structure within the octahedra. The XRD data of the temperature-treated PtNiMoRh-H octahedra still show two phases, a Pt-rich phase and a Ni-rich phase, and the STEM images still reveal the hexapod structure. The incorporation of Mo and Rh into PtNi octahedra can increase the stability of the particles through several mechanisms. Zhang *et al.* used density functional theory (DFT) calculations to investigate the influence of various transition metals on the segregation behaviour of Pt in Pt_3Ni. The authors considered factors such as surface energy, strain and heat of solution and their effect on Pt surface segregation energy in Pt_3Ni/M(111) surfaces.[45,46] Based on the Pt surface segregation energies, Rh shows a less negative value compared to Ni, suggesting that it suppresses Pt segregation more than Ni. Beermann *et al.* also confirmed the stabilising effect of rhodium experimentally by synthesising PtNi octahedra, enriching their surface with rhodium in a subsequent step and subjecting them to electrochemical ageing tests.[15,20] The PtNi octahedra surface-doped with rhodium showed hardly any loss of performance after the tests. Although this result is very promising, it cannot be fully applied to the heat-treated PtNiMoRh-H in this study, as molybdenum is used in addition to rhodium, which has been shown to contribute to the stabilisation of the octahedral shape. Moreover, unlike in Beermann's two-step synthesis, rhodium was introduced simultaneously with platinum and nickel in a one-pot approach here, which may have led to a different spatial distribution of Rh. The rhodium is probably located in the inner hexapod structure – based on the EDX images of the seeds formed after 2 h reaction time – and not exclusively on the octahedral surface, as well as due to the heat treatment and the associated surface restructuring. The finding that the Pt only segregated in the outermost layers indicates that either the stabilising effect of the rhodium and molybdenum was not sufficient in this area or that the two dopants are located inside the octahedron and primarily only stabilise the Pt-rich hexapod structure. This assumption is based on the fact that at the beginning of the synthesis of the PtNiMoRh particles, Pt and rhodium precursors are first reduced due to their noble character and form the hexapod structure. Only then are molybdenum and Ni reduced, forming the octahedral structure. The location of the rhodium within the Pt-rich hexapod skeleton of the octahedra provides a further explanation for the high stability of the octahedra: due to the stable Pt–Rh bond, Pt's tendency to segregate is moderately inhibited.[46,47] As a result, Pt and Ni are inhibited from mixing during heat treatment in the hexapod region, the hexapod structure is retained, stabilising the entire octahedron and the highly active {111} facets in particular. It is known that Mo mainly sits on the edges and corners of octahedrons and functions as a structural stabilizer. The shape of the octahedron is thus effectively stabilised by doping from the inside and outside.[14,39,48,49]

Effect of Pt skin formation on activity and stability

Based on the acquired electrochemical data the heat-treatment led to an increase in stability and, in the case of the doped material, to an increase in activity. The hydrogen induced Pt segregation resulted in the formation of a Pt skin with an

underlying Ni-rich layer. The Pt-skin structure typically exhibits higher catalytic activity compared to pure Pt or randomly alloyed PtNi surfaces. This is primarily due to the modified electronic structure of the surface Pt atoms. The underlying Ni-rich core induces strain in the Pt-skin layer, which alter the d-band centre of Pt atoms leading to optimised binding energies for oxygen and the ORR intermediates, enhancing catalytic performance.[4]

In the ORR, Pt–Ni alloys are hypothesised to optimise the binding strength of oxygen species on the catalyst surface. Pure Pt exhibits slightly stronger binding than ideal, but alloying with Ni is believed to modulate this interaction. Two key mechanisms are proposed to explain this effect. Firstly, electron transfer from Ni to Pt increases the occupancy of Pt 5d states, subsequently enhancing the filling of Pt–O antibonding orbitals formed between Pt 5d and O 2p. Secondly, the shift of Pt valence states to higher binding energies relative to the Fermi level is expected to further populate these antibonding orbitals. The combination of these electronic effects is postulated to weaken the Pt–O binding strength, potentially accounting for the observed enhancement in specific ORR activity across various Pt–Ni alloy compositions.[50]

Strasser showed using DFT, EXAFS and electrochemical measurements an increase in strain and in an optimal Pt to Ni ratio.[33] Both aspects led to enhanced oxygen adsorption properties of Pt and resulted in an acceleration of the ORR. Several groups have demonstrated the formation of a Pt-skin on PtNi and its excellent durability.[29,51,52] In all cases, it was observed that the formation of a protective Pt shell suppresses the leaching of Ni. Consequently, Ni poisoning of the surrounding Nafion is minimised and the preservation of the optimal Pt–Ni ratio in the outer shell of the catalyst particles is ensured, thereby maintaining the ligand and strain effects of the Ni on the oxygen adsorption properties of the Pt. Based on the STEM images revealing a Pt skin and the IL-STEM data showing no alteration of the PtNiMoRh-H particles following accelerated aging tests, it can be inferred that the Pt skin on the PtNiMoRh-H particles contributes significantly to their long-term stability. This protective layer is expected to enhance durability and maintain consistent activity even under realistic fuel cell conditions (80 °C and low pH).

Conclusions

In summary, the synthesis of Ni-rich PtNi and doped PtNiMoRh carbon-supported octahedral nanoparticles and the impact of a reductive heat-treatment on their electrochemical performance towards the ORR and their stability was investigated with RDE experiments, identical location STEM and *in situ* XRD and *in situ* environmental STEM. RDE experiments showed a substantial increase in activity and stability of the PtNi octahedra and their doped counterpart after the heat-treatment. For the first time, *in situ* high resolution STEM imaging showed the formation of Pt skin on the outermost layer due to heat-treatment in hydrogen at an atomic level. While the octahedral shape of the undoped PtNi was lost during heating and particle agglomeration was observed, the doped PtNiMoRh octahedra retained their shape. This observation was rationalised by a stabilising effect of rhodium on the hexapod structure inside the octahedra, which is mainly responsible for the octahedral shape during the synthesis of the catalyst. By maintaining the octahedral shape and by establishing an optimal Pt–Ni ratio on the particle surface and subsurface layers, ORR activity is increased and long-term stability is improved due to the protective outer Pt layer. Our comprehensive analysis demonstrates that controlled annealing in a hydrogen atmosphere serves as a powerful tool for precise surface engineering of catalysts. This process enables subtle modulation of surface–reactant binding energies, which in turn can lead to substantial enhancements in catalytic activity towards the ORR. The insights gained from this study have broad implications, potentially offering a versatile strategy for optimising the performance and longevity of diverse catalyst architectures by promoting tailored segregation of the desired active material to the catalysts surface.

Author contributions

Paul Paciok: conceptualization, investigation, methodology, data curation, formal analysis, visualization, writing – original draft, writing – review & editing. Shlomi Polani: conceptualization, investigation, methodology, writing – review & editing. Raffaele Amitrano: investigation, writing – review & editing. Tim Möller: investigation, writing – review & editing. Oleg Prymak: formal analysis, validation, writing – review & editing. Malte Klingenhof: investigation, data curation, visualization, writing – review & editing. H. Matsumoto: investigation, validation, writing – review & editing. K. MacArthur: conceptualization, investigation, writing – review & editing. J. Kang: investigation, formal analysis, writing – review & editing. Marc Heggen: conceptualization, supervision, funding acquisition, writing – review & editing. Peter Strasser: conceptualization, funding acquisition, supervision, writing – review & editing. Rafal E. Dunin-Borkowski: supervision, funding acquisition, writing – review & editing.

Data availability

All data supporting the findings of this study are available within the article and its supplementary information (SI). Supplementary information is available. See DOI: https://doi.org/10.1039/d5nr01964h.

Further details are available from the corresponding author upon reasonable request.

Conflicts of interest

There are no conflicts to declare.

Acknowledgements

The authors acknowledge financial support from the German Research Foundation (DFG) through grants HE 7192/1-2, STR 596/18-1, and STR 596/5-2, from the Federal Ministry of Education and Research (BMBF) *via* grant 03XP0251 ('KorrZellKat'), and from the Federal Ministry for Economic Affairs and Climate Action (BMWK) through grant 03ETB027H ('POREform'). The research leading to these results has received partial funding from the European Union's "Horizon Europe" Clean Hydrogen Partnership research and innovation program under grant agreement no. 101101409, BRAVA.

References

1 Y. Sun, S. Polani, F. Luo, S. Ott, P. Strasser and F. Dionigi, *Nat. Commun.*, 2021, **12**, 5984.
2 T. Asset, R. Chattot, M. Fontana, B. Mercier-Guyon, N. Job, L. Dubau and F. Maillard, *ChemPhysChem*, 2018, **19**, 1552–1567.
3 C. Lim, A. R. Fairhurst, B. J. Ransom, D. Haering and V. R. Stamenkovic, *ACS Catal.*, 2023, **13**, 14874–14893.
4 V. R. Stamenkovic, B. Fowler, B. S. Mun, G. Wang, P. N. Ross, C. A. Lucas and N. M. Marković, *Science*, 2007, **315**, 493–497.
5 V. R. Stamenkovic, B. S. Mun, M. Arenz, K. J. J. Mayrhofer, C. A. Lucas, G. Wang, P. N. Ross and N. M. Markovic, *Nat. Mater.*, 2007, **6**, 241–247.
6 J. Zhang, H. Yang, J. Fang and S. Zou, *Nano Lett.*, 2010, **10**, 638–644.
7 C. Cui, L. Gan, H.-H. Li, S.-H. Yu, M. Heggen and P. Strasser, *Nano Lett.*, 2012, **12**, 5885–5889.
8 S.-I. Choi, S. Xie, M. Shao, J. H. Odell, N. Lu, H.-C. Peng, L. Protsailo, S. Guerrero, J. Park, X. Xia, J. Wang, M. J. Kim and Y. Xia, *Nano Lett.*, 2013, **13**, 3420–3425.
9 C. Cui, L. Gan, M. Heggen, S. Rudi and P. Strasser, *Nat. Mater.*, 2013, **12**, 765–771.
10 K. E. Macarthur, M. Heggen and R. E. Dunin-Borkowski, *Adv. Struct. Chem. Imaging*, 2018, **4**, 2.
11 L. Gan, C. Cui, M. Heggen, F. Dionigi, S. Rudi and P. Strasser, *Science*, 2014, **346**, 1502–1506.
12 F. Xiao, X. Qin, M. Xu, S. Zhu, L. Zhang, Y. Hong, S.-I. Choi, Q. Chang, Y. Xu, X. Pan and M. Shao, *ACS Catal.*, 2019, **9**, 11189–11198.
13 Y. Li, F. Quan, L. Chen, W. Zhang, H. Yu and C. Chen, *RSC Adv.*, 2014, **4**, 1895–1899.
14 X. Huang, Z. Zhao, L. Cao, Y. Chen, E. Zhu, Z. Lin, M. Li, A. Yan, A. Zettl, Y. M. Wang, X. Duan, T. Mueller and Y. Huang, *Science*, 2015, **348**, 1230–1234.
15 V. Beermann, M. Gocyla, E. Willinger, S. Rudi, M. Heggen, R. E. Dunin-Borkowski, M.-G. Willinger and P. Strasser, *Nano Lett.*, 2016, **16**, 1719–1725.
16 E. Hornberger, M. Klingenhof, S. Polani, P. Paciok, A. Kormányos, R. Chattot, K. E. Macarthur, X. Wang, L. Pan, J. Drnec, S. Cherevko, M. Heggen, R. E. Dunin-Borkowski and P. Strasser, *Chem. Sci.*, 2022, **13**, 9295–9304.
17 M. Ronovský, O. Dunseath, T. Hrbek, P. Kúš, M. Gatalo, S. Polani, J. Kubát, D. Götz, H. Nedumkulam, A. Sartori, E. Petrucco, F. Ruiz-Zepeda, N. Hodnik, A. M. Bonastre, P. Strasser and J. Drnec, *ACS Energy Lett.*, 2024, **9**, 5251–5258.
18 S. Polani, R. Amitrano, A. F. Baumunk, L. Pan, J. Lu, N. Schmitt, U. Gernert, M. Klingenhof, S. Selve, C. M. Günther, B. J. M. Etzold and P. Strasser, *ACS Appl. Mater. Interfaces*, 2024, **16**, 52406–52413.
19 M. Ahmadi, F. Behafarid, C. Cui, P. Strasser and B. R. Cuenya, *ACS Nano*, 2013, **7**, 9195–9204.
20 L. Pan, A. Parnière, O. Dunseath, D. Fongalland, G. Nicolau, C. C. Weber, J. Lu, M. Klingenhof, A. Arinchtein, H.-S. Oh, P.-Y. Blanchard, S. Cavaliere, M. Heggen, R. E. Dunin-Borkowski, A. M. Bonastre, F. Dionigi, J. Sharman, D. Jones and P. Strasser, *ACS Catal.*, 2024, **14**, 10–20.
21 S. Polani, K. E. Macarthur, M. Klingenhof, X. Wang, P. Paciok, L. Pan, Q. Feng, A. Kormányos, S. Cherevko, M. Heggen and P. Strasser, *ACS Catal.*, 2021, **11**, 11407–11415.
22 L. Gan, M. Heggen, C. Cui and P. Strasser, *ACS Catal.*, 2016, **6**, 692–695.
23 K. E. Macarthur, S. Polani, M. Klingenhof, N. Gumbiowski, T. Möller, P. Paciok, J. Kang, M. Epple, S. Basak, R.-A. Eichel, P. Strasser, R. E. Dunin-Borkowski and M. Heggen, *ACS Appl. Energy Mater.*, 2023, **6**, 5959–5967.
24 O. L. Krivanek, M. F. Chisholm, V. Nicolosi, T. J. Pennycook, G. J. Corbin, N. Dellby, M. F. Murfitt, C. S. Own, Z. S. Szilagyi, M. P. Oxley, S. T. Pantelides and S. J. Pennycook, *Nature*, 2010, **464**, 571–574.
25 B. Danisman, G. R. Zhang, A. F. Baumunk, J. Yang, O. Brummel, P. Darge, D. Dworschak, K. J. J. Mayrhofer, J. Libuda, X. Zhou, M. Wu, E. Spiecker, M. Ledendecker and B. J. M. Etzold, *ChemElectroChem*, 2024, **11**, e202400070.
26 B. Danisman, G. R. Zhang, A. F. Baumunk, J. Yang, O. Brummel, P. Darge, K. J. J. Mayrhofer, J. Libuda, M. Ledendecker and B. J. M. Etzold, *ChemElectroChem*, 2023, **10**, e202300109.
27 G. M. Leteba, D. R. G. Mitchell, P. B. J. Levecque, L. Macheli, E. van Steen and C. I. Lang, *ACS Appl. Nano Mater.*, 2020, **3**, 5718–5731.
28 D. F. van der Vliet, C. Wang, D. Li, A. P. Paulikas, J. Greeley, R. B. Rankin, D. Strmcnik, D. Tripkovic, N. M. Markovic and V. R. Stamenkovic, *Angew. Chem., Int. Ed.*, 2012, **51**, 3139–3142.
29 N. Becknell, Y. Kang, C. Chen, J. Resasco, N. Kornienko, J. Guo, N. M. Markovic, G. A. Somorjai, V. R. Stamenkovic and P. Yang, *J. Am. Chem. Soc.*, 2015, **137**, 15817–15824.
30 T. Shinagawa, A. T. Garcia-Esparza and K. Takanabe, *Sci. Rep.*, 2015, **5**, 13801.
31 C. Chen, Y. Kang, Z. Huo, Z. Zhu, W. Huang, H. L. Xin, J. D. Snyder, D. Li, J. A. Herron, M. Mavrikakis, M. Chi,

K. L. More, Y. Li, N. M. Markovic, G. A. Somorjai, P. Yang and V. R. Stamenkovic, *Science*, 2014, **343**, 1339–1343.
32 M. Vega-Paredes, R. Aymerich-Armengol, D. Arenas Esteban, S. Martí-Sánchez, S. Bals, C. Scheu and A. Garzón Manjón, *ACS Nano*, 2023, **17**, 16943–16951.
33 P. Strasser, S. Koh, T. Anniyev, J. Greeley, K. More, C. Yu, Z. Liu, S. Kaya, D. Nordlund, H. Ogasawara, M. F. Toney and A. Nilsson, *Nat. Chem.*, 2010, **2**, 454–460.
34 X. Luo, Y. Guo, H. Zhou, H. Ren, S. Shen, G. Wei and J. Zhang, *Front. Energy*, 2020, **14**, 767–777.
35 S. Xu, E. D. Walter, Z. Zhao, M. Y. Hu, X. Han, J. Z. Hu and X. Bao, *J. Phys. Chem. C*, 2015, **119**, 21219–21226.
36 R. Mu, Q. Fu, H. Liu, D. Tan, R. Zhai and X. Bao, *Appl. Surf. Sci.*, 2009, **255**, 7296–7301.
37 Q. Jeangros, T. W. Hansen, J. B. Wagner, C. D. Damsgaard, R. E. Dunin-Borkowski, C. Hébert, J. Van Herle and A. Hessler-Wyser, *J. Mater. Sci.*, 2013, **48**, 2893–2907.
38 J. T. Richardson, R. Scates and M. V. Twigg, *Appl. Catal., A*, 2003, **246**, 137–150.
39 Q. Wang, B. Zhu, F. Tielens, D. Tichit and H. Guesmi, *Appl. Surf. Sci.*, 2021, **548**, 149217.
40 W. Yu, M. D. Porosoff and J. G. Chen, *Chem. Rev.*, 2012, **112**, 5780–5817.
41 D. S. R. Rocabado, Y. Nanba and M. Koyama, *Comput. Mater. Sci.*, 2020, **184**, 109874.
42 R. Tran, Z. Xu, B. Radhakrishnan, D. Winston, W. Sun, K. A. Persson and S. P. Ong, *Sci. Data*, 2016, **3**, 160080.
43 Y. Yang, J. Zhou, Z. Zhao, G. Sun, S. Moniri, C. Ophus, Y. Yang, Z. Wei, Y. Yuan, C. Zhu, Y. Liu, Q. Sun, Q. Jia, H. Heinz, J. Ciston, P. Ercius, P. Sautet, Y. Huang and J. Miao, *Nat. Catal.*, 2024, **7**, 796–806.
44 S. Horch, H. T. Lorensen, S. Helveg, E. Lægsgaard, I. Stensgaard, K. W. Jacobsen, J. K. Nørskov and F. Besenbacher, *Nature*, 1999, **398**, 134–136.
45 N. Zhang, Q. Shao, X. Xiao and X. Huang, *Adv. Funct. Mater.*, 2019, **29**, 1808161.
46 Y. Zhang, Z. Duan, C. Xiao and G. Wang, *Surf. Sci.*, 2011, **605**, 1577–1582.
47 O. Ozturk, J. B. Park, S. Ma, J. S. Ratliff, J. Zhou, D. R. Mullins and D. A. Chen, *Surf. Sci.*, 2007, **601**, 3099–3113.
48 L. Cao and T. Mueller, *Nano Lett.*, 2016, **16**, 7748–7754.
49 Q. Jia, Z. Zhao, L. Cao, J. Li, S. Ghoshal, V. Davies, E. Stavitski, K. Attenkofer, Z. Liu, M. Li, X. Duan, S. Mukerjee, T. Mueller and Y. Huang, *Nano Lett.*, 2018, **18**, 798–804.
50 J. Chen, Y. Z. Finfrock, Z. Wang and T.-K. Sham, *Sci. Rep.*, 2021, **11**, 13698.
51 Y. Zhuang, Y. Iguchi, T. Li, M. Kato, Y. A. Hutapea, A. Hayashi, T. Watanabe and I. Yagi, *ACS Catal.*, 2024, **14**, 1750–1758.
52 Y. Wang, S. Chen, X. Wang, A. Rosen, W. Beatrez, L. Sztaberek, H. Tan, L. Zhang, C. Koenigsmann and J. Zhao, *ACS Appl. Energy Mater.*, 2020, **3**, 768–776.